Inorg. Chem. **2004**, *43*, 4708–4718

XAFS and LIBD Investigation of the Formation and Structure of Colloidal Pu(IV) Hydrolysis Products

Jörg Rothe, Clemens Walther, Melissa A. Denecke,* and Th. Fanghänel

Institut für Nukleare Entsorgung, Forschungszentrum Karlsruhe, Postfach 3640, D-76021 Karlsruhe, Germany

Received February 3, 2004

Pu(IV) oxyhydroxide colloid growth is investigated with XAFS and LIBD. From combined results a model of colloid formation is proposed, which leads to a face-centered cubic Pu sublattice having cation defects, as observed with EXAFS, and a linear dependency of log [Pu(IV)] on –log [H^+] with slope –2, in accord with LIBD. The solubility for Pu(IV) measured with LIBD is close to the lower limit of the solubility curve from previously reported data.

Introduction

Reports of X-ray absorption fine structure (XAFS) studies on the formation of actinide oxyhydroxide "eigen-colloids" including Pu L-edge XAFS investigations of Pu(IV) eigen-colloids are sparse. Conradson[1] describes a low-temperature XAFS investigation of Pu(IV) oxyhydroxide colloids, isolated from solution via centrifugation, reporting observation of multiple, distinct Pu−O bonds due to the presence of different Pu−O moieties. Understanding the mechanism of Pu(IV) "eigen-colloid" formation is important, e.g., for understanding the origin of variations in results of Pu(IV) solubility studies reported in the literature[2−5] and why apparent nonlinear behavior of Pu(IV) solubility in the millimole range at −log [H^+] approaching zero has been reported.[4] Such information is not solely of interest to basic research but has technological significance. For example, the solubility of Pu(IV) in groundwater is an important aspect in the performance and safety of sites for nuclear waste disposal in deep geological formations.

In this paper we report on the structures of colloids formed upon increasing the −log [H^+] of an aqueous Pu(IV) solution through dilution and, in one case, addition of NaOH, characterized from their Pu L3 extended X-ray absorption fine structure (EXAFS) spectra. In addition, their valence and electronic structure near the continuum are evaluated from their Pu L3 X-ray absorption near edge structure (XANES). The colloids are studied without prior separation from solution and compared to results for freshly precipitated amorphous $Pu(OH)_4$(am) and the Pu^{4+} aquo ion.

Independently, Pu(IV) oxyhydroxide colloids are investigated by laser induced breakdown detection (LIBD). We have studied the onset of eigen-colloid formation in an initially colloid free Pu(IV) solution as it is continually diluted. The −log [H^+] and Pu(IV) concentration at which colloids form, as detected by an increase in the LIBD signal, is an indicator as the point crossing over the solubility limit.

Experimental Section

XAFS Sample Preparation. The samples investigated are indicated with capital, bold-face letters in the solubility diagram for Pu(IV) in Figure 1 and summarized in Table 1. Samples **C** through **H** are prepared from a Pu(IV) solution designated sample **A**. Solution sample **A** is prepared from a ^{242}Pu(VI) stock solution by bubbling NO through it. The concentration of the Pu(VI) stock solution is determined prior to reduction from its UV/vis absorption spectrum to be 16.1 mM Pu(VI). Utmost care was taken to avoid oxygen in the samples. All of the aqueous reagents were prepared from oxygen free water. The Pu(IV) solution samples are prepared in a N_2 purged glovebag by appropriate addition of aqueous solutions of milli-Q water, 0.5 M HCl, 1.25 M NaCl, and (only for sample **G**) 1 M NaOH. Sample **F** is prepared by dilution of 111 μL acidic aqueous 16.1 mM Pu(IV) with 889 μL of 0.5 M NaCl. The −log [H^+] values for XAFS samples in Table 1 are measured with a Ross electrode following calibration with commercial reference buffer solutions having −log [H^+] of 4.00 and 7.01. Following the experiments, a control UV/vis measurement of sample **A** is performed. The spectra indicate that the solution contains colloids, but no evidence of oxidation is observed. Sample **B** is produced by electrochemical reduction of a mixture of a different

* To whom correspondence should be addressed. Tel: +49 7247 82 5536. Fax: +49 7247 82 3927. E-mail: Melissa.Denecke@ine.fzk.de.

(1) Conradson, S. D. *Appl. Spectrosc.* **1998**, *52* (7), 252−279.
(2) Fujiwara, K.; Yamana, H.; Fujii, T.; Moriyama, H. *J. Nucl. Fuel Cycle Environ. (Japan)* **2001**, *7*, 17−23.
(3) Capevila, H.; Vitorge, P. *Radiochim. Acta* **1998**, *82*, 11−16.
(4) Kim, J. I.; Kanellakopulos, B. *Radiochim. Acta* **1989**, *48*, 145−150.
(5) Rai, D. *Radiochim. Acta* **1984**, *35*, 97−106.

10.1021/ic049861p CCC: $27.50
Published on Web 06/24/2004

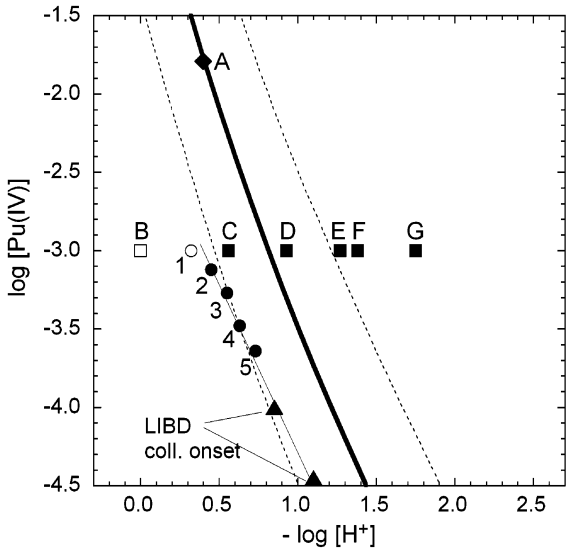

Figure 1. Solubility curve of Pu(IV) using log $K^{\circ}_{sp} = -58.7 + -0.3$ from ref 32. Square symbols marked with letters indicate composition (Pu(IV) concentrations and $-\log [H^+]$) of XAFS solution samples, and circles marked with numbers LIBD samples investigated. Triangles show points of colloid formation observed in analogous dilution series LIBD studies at Pu concentrations lower than 1 mM. See text for details.

Table 1. Summary of Samples Examined by XAFS and LIBD in This Study

ID	sample description
A	16.1 mM Pu(IV) in 0.4 M HCl
B	1 mM Pu(IV) in 1 M $HClO_4$, $-\log [H^+] = 0$
C	1 mM Pu(IV) in 0.5 M NaCl, $-\log [H^+] = 0.56$
D	1 mM Pu(IV) in 0.5 M NaCl, $-\log [H^+] = 0.93$
E	1 mM Pu(IV) in 0.5 M NaCl, $-\log [H^+] = 1.27$
F	1.22 mM Pu(IV) in 0.5 M NaCl, $-\log [H^+] = 1.38$
G	1 mM Pu(IV) in 0.5 M NaCl, $-\log [H^+] = 1.75$
H	precipitated $Pu(OH)_4$ (am)
1	1 mM Pu(IV), I = 0.5 M, $-\log [H^+] = 0.32$
2	0.76 mM Pu(IV), I = 0.5 M, $-\log [H^+] = 0.45$
3	0.54 mM Pu(IV),, I = 0.5 M, $-\log [H^+] = 0.55$
4	0.33 mM Pu(IV), I = 0.5 M, $-\log [H^+] = 0.63$
5	0.23 mM Pu(IV), I = 0.5 M, $-\log [H^+] = 0.73$

^{242}Pu stock solution in 1 M $HClO_4$ to Pu(III) and subsequent oxidation to Pu(IV). The total Pu concentration is assayed by liquid scintillation counting and the tetravalent oxidation state purity also verified by absorption spectroscopy. The amorphous $Pu(OH)_4$(am) (sample **H**) is freshly precipitated from approximately 1 mM Pu(IV) solution by addition of 1 M NaOH to $-\log [H^+]$ between approximately 2.0 and 2.3. The solid is separated from the aqueous solution by ultrafiltration and collected on a cellulose triacetate membrane microfilter (Amicron, area: 10 kDalton, average pore size radius ~1.5 nm). The filter with the wet solid is encased inside a thin latex bag. The solution samples are contained in capped polyethylene vials (4 mm inner diameter), with the caps taped with a thick layer of Parafilm to prevent oxygen intrusion or evaporation. XAFS measurements are performed two to four days after sample preparation.

XAFS Data Acquisition and Analysis. XAFS measurements of samples **A** and **C** through **H** are performed at the Advanced Photon Source (APS), at the BESSRC beamline 12BM, using a Si(111) double-crystal monochromator (DCM). The 12BM beamline is equipped with a collimating and focusing mirror, and the beam spot used is 0.5 mm^2. The incident beam is free of higher harmonic reflections, as is shown by the absence of the corresponding inelastic scattering peaks recorded with an energy dispersive detector. The spectra are calibrated against the first derivative XANES spectrum of a Zr foil, defined as 17.998 keV. Spectra are recorded in both transmission and fluorescence mode. Argon filled ionization chambers are used for transmission spectra detection, and a 13-element energy dispersive solid state Ge detector is used for fluorescence spectra. Samples are studied mounted in the Actinide Facility sample changer[6] for transport and measurement. Three to seven scans are collected and averaged for each sample.

Pu L3 edge XAFS data for sample **B** is collected at the Rossendorfer Beamline (ROBL), BM20, at the European Synchrotron Radiation Facility (ESRF). A 5-element energy dispersive solid state Ge detector is used for fluorescence detection. A Si(111) crystal pair is used in the DCM, and the energy scale is also calibrated against the first derivative XANES spectrum of a Zr foil, as for the samples measured at APS.

EXAFS data analysis is based on standard least-squares fit techniques[7] using the WinXAS[8] and the UWXAFS[9] program packages. The region up to about 700 eV above the Pu L3 edge ($k \sim 13$ Å^{-1}) is investigated. The atomic background function $\mu_0(E)$ is optimized with respect to spurious contributions below ~1 Å in the k^2-weighted Fourier transform (FT) of the data using WinXAS. The ionization energy E_0, the origin for calculation of the $\chi(k)$ function, is fixed at the maximum of the most intense absorption feature—the white line (WL)—in the individual spectra at ~18068 eV. Metric parameters (neighboring atomic distances R_i, mean square radial displacements or EXAFS Debye−Waller factors σ^2_i, and coordination numbers N_i for the different coordination shells i) are determined using the feffit code. Backscattering amplitude and phase shift functions for single scattering paths in a 3-shell PuO_2 cluster (*Fm*3*m* fluorite structure with a lattice constant of 5.396 Å[10]) are obtained from FEFF8.2[11,12] calculations. Prior to analysis, the k^2-weighted EXAFS spectra are Fourier transformed over a k-space range of ~2.7−12.5 Å^{-1}, using symmetric square windows with $\Delta k = 0.2$ Å^{-1} "Hanning sills". All fitting operations are performed in R-space over the individual radial distance ranges given in Table 2. Special care is taken to avoid overinterpretation of the data beyond the limits defined by the number of independent points.[13] The amplitude reduction factor[14] S_0^2 is fixed at 1. Martin et al.[15] applied S_0^2 0.9 in order to reproduce the theoretical coordination number (8) for the first oxygen neighbor shell in the PuO_2 fluorite structure.

The *feffit* code evaluates randomly distributed fit uncertainties as the amount by which a given parameter changes, when values for all other parameters remain fixed, while maintaining the sum of squares of the difference between data and model (Chi^2) below a certain limit (as suggested by Teo[13]). This procedure yields uncertainty values for the nearest neighbor oxygen shell of $\Delta R_O \leq 0.02$ Å and $\Delta N_O \leq 0.4$ for samples **B**, **C**, and **H**, which are modeled

(6) See: http://chemistry.anl.gov:80/heavy-element/actinide/multiple.html (accessed June 2004).
(7) Sayers, D. E.; Bunker, B. A. In *X-Ray Absorption: Techniques of EXAFS, SEXAFS and XANES*; Koningsberger, D. C., Prins, R., Eds.; J. Wiley & Sons: New York, 1988; pp 211−253.
(8) Ressler, T. *J. Phys. IV* **1997**, *7-C2*, 269.
(9) Stern, E. A.; Newville, M.; Ravel, B.; Yacoby, Y.; Haskel, D. *Physica B* **1995**, *208&209*, 117−120.
(10) See: http://www.mrw.interscience.wiley.com/ueic/articles/a21_133/frame.html.
(11) Ankudinov, A. L.; Ravel, B.; Rehr, J. J.; Conradson, S. D. *Phys. Rev. B* **1998**, *58*, 7565−7576.
(12) Ankudinov, A. L.; Rehr, J. J. *Phys. Rev. B* **1997**, *56*, 1712.
(13) Teo, B.-K. *EXAFS: Basic Principles and Data Analysis*; Springer-Verlag: Heidelberg, 1988.
(14) Lee, P. A.; Citrin, P. H.; Eisenberger, P.; Kincaid, B. M. *Rev. Mod. Phys.* **1981**, *53*, 769−806.
(15) Martin, P.; Grandjean, S.; Ripert, M.; Freyss, M.; Blanc, P.; Petit, T. *J. Nucl. Mater.* **2003**, *320*, 138−141.

Table 2. Data Range and Metric Parameters Extracted by Least-Squares Fit of EXAFS Spectra to the EXAFS Equation[a]

ID	fit range $R-\Delta$ (Å)	shell	R (Å)	N	σ^2 (Å^2)	ΔE (eV)	R-factor
A	1.34−4.02	O1	2.24	3.3	0.0031	3.07	0.005
		O2	2.42	0.8	0.0099	3.07	
		Pu	3.86	2.1	0.0076	3.19	
B	1.32−2.67	O	2.38	8.4	0.0077	8.3	0.004
C	1.32−4.08	O	2.35	7.2	0.0094	1.06	0.007
		Pu	3.90	1.9	0.0067	4.64	
D	1.35−4.0	O1	2.20[b]	1.1	0.0004	3.10	0.007
		O2	2.42	4.4	0.0068	3.10	
		Pu	3.90	3.0	0.0085	4.52	
E	1.32−3.96	O1	2.22	0.7	0.0012	2.77	0.013
		O2	2.38	5.6	0.0122	2.77	
		Pu	3.85	4.3	0.0090	2.08	
F	1.35−3.99	O1	2.22	1.5	0.0017	2.51	0.008
		O2	2.39	4.0	0.0059	2.51	
		Pu	3.87	4.2	0.0075	1.71	
G	1.32−3.96	O1	2.29	1.4	0.0080	3.08	0.008
		O2	2.37	5.0	0.0136	3.08	
		Pu	3.87	4.9	0.0075	1.74	
H	1.35−3.99	O	2.32	4.0	0.0104	2.38	0.016
		Pu	3.87	2.4	0.0066	1.84	

[a] See text for error discussion. S_0^2 fixed at 1.0. [b] Denotes fixed value.

using a single oxygen shell. However, in the case of samples **A**, **D**, **E**, **F**, and **G** the strong correlation between the two oxygen shells required for modeling the highly asymmetric neighboring oxygen contributions leads to much higher ΔR_{O1}, ΔR_{O2}, ΔN_{O1}, and ΔN_{O2} values, reflecting the shallow minimum of the fit in a multiple parameter space. Determination of fit parameters for the more distant plutonium backscatterers yields $\Delta R_{Pu} \leq 0.04-0.08$ Å and $\Delta N_{Pu} \leq 1.2$ for samples **A**, **C**, **D**, **E**, **F**, **G**, and **H**. The overall goodness of the fit evaluated by *feffit* is given as the "*R*-factor" (listed in the last column in Table 2), which is Chi^2 scaled by the magnitude of data.[16] $R = 0.02$ signifies that the average deviation between theory and data is two percent.

XANES spectra for samples **A**−**H** are isolated from XAFS scans following subtraction of the preedge background absorption, approximated as a linear function, and normalization of the edge jump (average between 18100 and 18300 eV) to unity. In order to quantify the WL intensity in these spectra, curve-fitting is accomplished by modeling the experimental data using pseudo-Voigt (WL), Gaussian (feature near 18105 eV), and arctan (edge-step) functions. The arctan width is set to the natural Pu L3 line width,[17] whereas the arctan position for samples **A** and **C**−**H** is fixed to the fit value obtained for sample **B**.

LIBD Measurements. The LIBD technique has been described previously[18,19] and shall only be discussed briefly. A pulsed laser is focused into the colloidal suspension and a plasma is ignited selectively when the laser power is great enough and a colloid is present in the focal region. Detecting the plasma by means of its shock wave is hence equivalent to counting colloids. By varying the laser pulse energy, the mean size and number-concentration of colloids can be quantified.[20] Particles down to 5 nm in size can be detected at concentrations well below 10^{-8} M.

The colloid samples investigated with LIBD are indicated with boldface numbers **1** through **5** in Figure 1 and listed in Table 1. Solution **1** is prepared electrolytically similarly to the XAFS sample **B** but using a ^{242}Pu stock solution in 0.5 M HCl. This solution **1** is observed from LIBD measurements to be colloid free at log [Pu] −3.0 and −log [H$^+$] 0.32 (Figure 1, open circle). The −log [H$^+$] of the solution is increased very slowly by dilution with 0.5 M NaCl (<10 μL/min). At the same time, dilution with the NaCl solution also causes a decrease in Pu(IV) concentration. At −log [H$^+$] 0.45, the onset of Pu(IV) colloid formation is observed as a well-defined, sharp increase of the LIBD signal (sample **2**, filled circles). Further dilution of the Pu(IV) solution leads to the colloidal samples **3** through **5** in Figure 1. Analogous dilution series are measured beginning at Pu(IV) concentrations lower than log [Pu] −3.0, and the points of colloid formation are included in Figure 1 (filled triangles). We would like to stress that there is no precipitate or bulk plutonium phase in the classical sense present in these samples during LIBD measurements. The only solid plutonium present is the suspended colloids. Consequently, the thermodynamic equilibrium between solvated Pu(IV) and bulk in a classical solubility study is substituted by an equilibrium between colloidal fraction and solute species in an LIBD experiment.

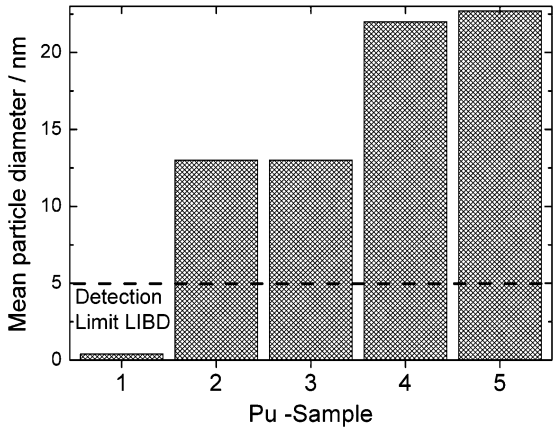

Figure 2. Mean particle diameter for colloids larger than 5 nm (limit of detection) in samples **1** through **5**, as determined with LIBD.

Results

LIBD Measurements. From the LIBD measurements a mean particle diameter for colloids larger than 5 nm (detection limit) is obtained. Figure 2 shows the mean colloid diameter found for samples **1** through **5**. Sample **1** is "colloid free" in the sense that no colloids larger than 5 nm are present. The colloids in samples **2** and **3** are around 12 nm in size. The ones in samples **4** and **5** are almost twice as large.

EXAFS Results. The k^2-weighted EXAFS-functions $\chi(k)$, extracted using WinXAS, are shown in Figure 3 at the left, and the corresponding FT magnitudes are shown at the right-hand side. All spectra exhibit an intense, more or less asymmetric FT peak at ∼1.9 Å, corresponding to a phase corrected distance value of about 2.4 Å. This peak represents oxygen atoms comprising the first coordination sphere of the central absorbing Pu(IV) in all samples. Additional peaks or shoulders at about 1.15−1.2 Å, representing a low frequency contribution to the EXAFS, are obvious for all spectra. These features are apparently not an artifact of the μ_0 spline function subtraction, because they are persistent

(16) Newville, M. *FEFFIT—Using FEFF to model XAFS data*; Department of Physics, FM-15, University of Washington: Seattle, 1995.
(17) Krause, M. O.; Oliver, J. H. *J. Phys. Chem. Ref. Data* **1979**, *8*, 329.
(18) Scherbaum, F. J.; Knopp, R.; Kim, J. I. *Appl. Phys. B* **1996**, *63*, 299−306.
(19) Kitamori, T.; Yokose, K.; Sakagami, M.; Sawada, T. *Jpn. J. Appl. Phys.* **1989**, *28*, 1195−1198.
(20) Walther, C.; Bitea, C.; Hauser, W.; Kim, J. I.; Scherbaum, F. J. *Nucl. Instrum. Methods B* **2002**, *195*, 374−388.

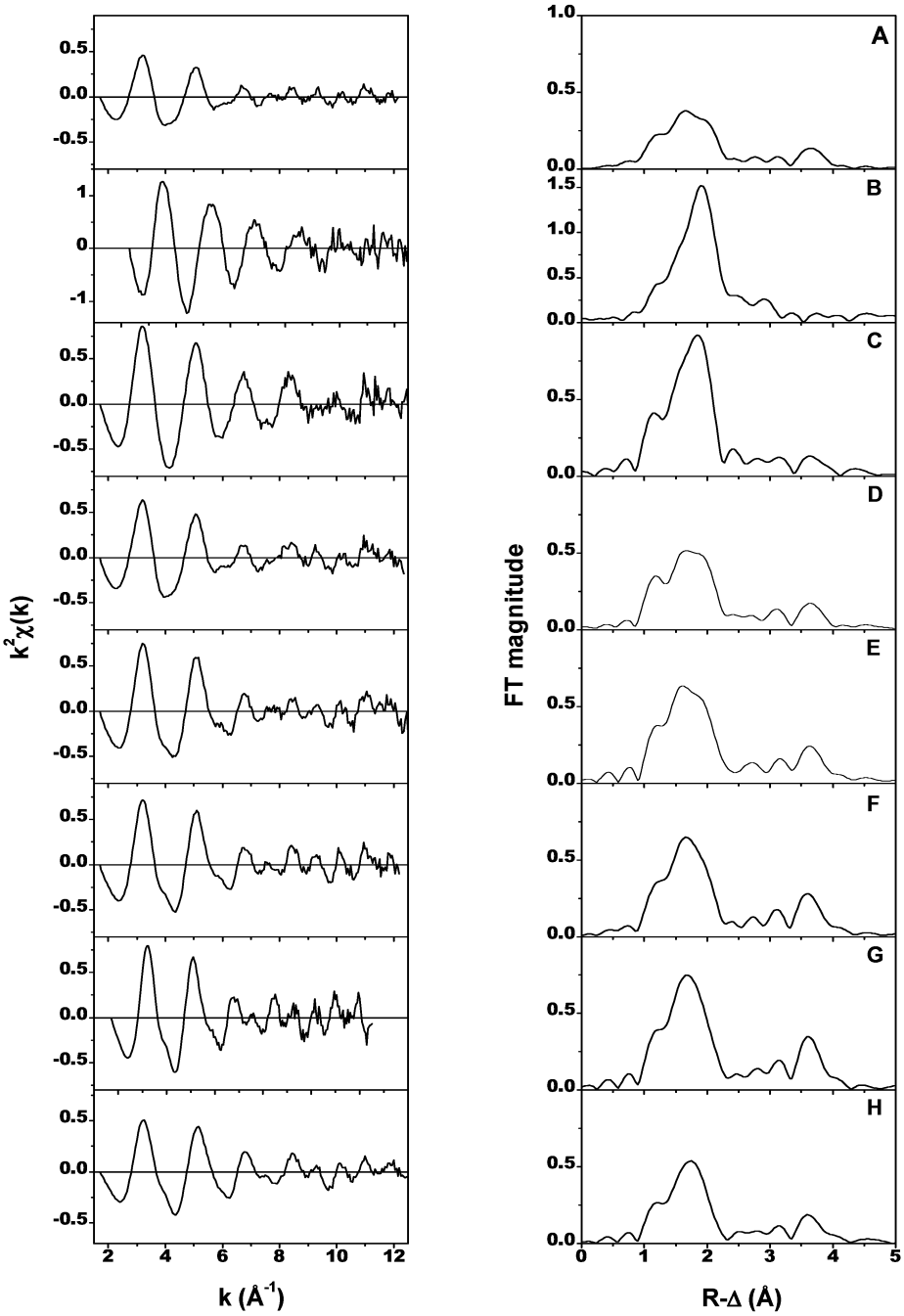

Figure 3. k^2-weighted $\chi(k)$-functions of the samples listed in Table 1 (left panel) and corresponding Fourier transform magnitudes (right panel). Note the different ordinate scale for sample **B**.

in the FT spectra, except for cases where the μ_0 spline is allowed to be flexible as to intolerably remove intensity from the Pu−O peak at $R - \Delta = 1.9$ Å. Other Pu L3 edge EXAFS presented in the literature, including data taken at different experimental stations, also show these low-R features in the FT spectra (see, e.g., ref 21). A Pu−O distance of less than 2 Å makes no physical sense (the sum of ionic radii is 2.26 Å for Pu(IV) with 6-fold coordination[22]), so that we expect these features to be due to atomic contributions or to multielectron excitations in the EXAFS regime.[23] Supporting the latter hypothesis, the FEFF8.2 calculation using a three-shell (45 atom) PuO_2 cluster in Cartesian coordinates displays an energy dependence of μ_0 with discontinuities, evidence for multielectron excitations.[24] Despite its continual presence, inclusion or omission of this low-R feature by broadening or narrowing the R-space fit range does not significantly influence the fit results.

The EXAFS metrical parameters obtained from fits of the EXAFS equation to the experimental data are summarized in Table 2. Figures 4 and 5 display experimental data and the fit results in R-space and backtransformed k-space for

(21) Richmann, M. K.; Reed, D. T.; Kropf, A. J.; Aase, S. B.; Lewis, M. A. *J. Nucl. Mater.* **2001**, *297*, 303−312.
(22) Greenwood, N. N.; Earnshaw, A. *Chemie der Elemente*; VCH Verlagsgesellschaft: Weinheim, 1988.
(23) Wang, W.-C.; Yu, C. *Phys. Status Solidi A* **1998**, *168*, 351−357.
(24) Rehr, J. J.; Zabinsky, S. I.; Ankudinov, A.; Albers, R. C. *Physica B* **1995**, *208&209*, 23−26.

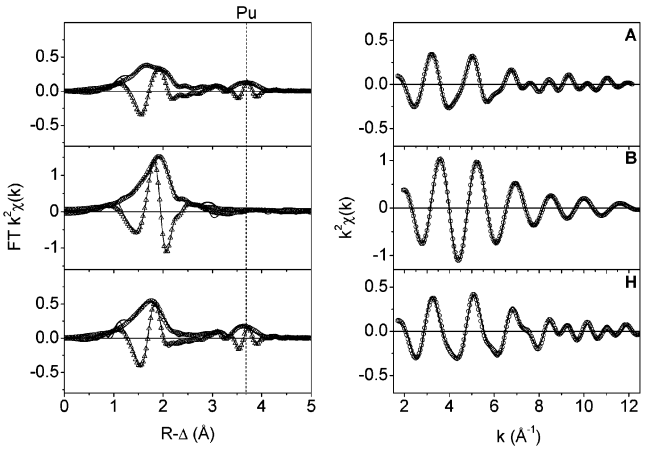

Figure 4. *R*-space fit results for samples **A**, **B**, **H**. Left panel: FT magnitude of EXAFS data (solid line), fit magnitude (open circles), FT imaginary part (thin solid line), and fit imaginary part (open triangles). Right panel: corresponding Fourier-filtered data (solid line, ranges given in Table 2) and backtransformed fit (open circles). Note the different ordinate scale for sample **B**. Dashed line marks Pu−Pu interaction.

the sample spectra, segregated into two groups. The first group (samples **A**, **B**, and **H**, Figure 4) includes the stock solution and reference compounds (Pu^{4+} aquo ion and solid $Pu(OH)_4$(am) precipitate), whereas the second group (samples **C**−**G**, Figure 5) tracks the fate of the colloidal suspensions after crossing the solubility threshold when successively increasing −log [H^+]. The presentation of the results below is structured according to these two groups of sample sets.

Only sample **B** (1 mM Pu(IV) in 1 M $HClO_4$, −log [H^+] 0) exhibits a spectrum dominated by a single sinusoidal contribution, originating from backscattering on a single shell of oxygen atoms. Sample **A,** the Pu(IV) stock solution, as well as the solid sample **H** and the colloidal suspensions **C**−**G** exhibit a more complex absorption fine structure. This includes the appearance of a high-frequency EXAFS contribution, which is found in the fit procedure to be associated with a Pu−Pu interaction.

Samples A, B, H. The experimental FT magnitudes and fits for samples **A**, **B**, and **H** and their corresponding Fourier-filtered data are shown in Figure 4. The EXAFS spectrum for solution **B** exhibits the signature of the Pu^{4+} aquo ion[25] with ∼8 oxygen atoms at 2.38 Å and $\sigma^2 = 0.0077$ Å^2 (Table 2). The spectra of the amorphous precipitate (sample **H**) and the aqueous stock solution (sample **A**, 16.1 mM Pu(IV) in 0.4 M HCl) exhibit more complex structures. Above the spurious low-*R* feature, the major oxygen FT peak appears strongly dampened and broadened as compared to the aquo ion (note the different ordinate scale for sample **B** in Figure 4). An additional FT peak surmounting the noise level is observed in both spectra between about 3.3 and 4.1 Å. In contrast to samples **B** and **H**, we did not succeed in modeling the FT of sample **A** between 1.34 and 2.32 Å using a single shell of oxygen backscatterers. Addition of a second oxygen scattering path (O2) leads to a reasonable fit for sample **A** with about three oxygen atoms at 2.24 Å and ∼1 further distant oxygen atom at 2.42 Å. ΔE_0 for the two adjacent oxygen shells is confined to the same value. The large asymmetry of the Pu−O shell in sample **H** is reflected by a σ^2 value of >0.01 Å^2. A large σ^2 value is also obtained in the fit when an additional asymmetry term is added (third cumulant). The apparent number of coordinating oxygen atoms (∼4) obtained for samples **A** and **H** is reduced by 50% compared to the aquo ion and the theoretical value of 8 expected for crystalline PuO_2. There is good agreement between FT imaginary part and magnitude of the fit and the experimental feature located between 3.3 and 4.1 Å (dashed line in Figure 4) using a Pu−Pu interaction for samples **A** and **H**. In both samples Pu coordination numbers (2.1 and 2.4) and Pu−Pu second next-neighbor distances (3.86 and 3.87 Å) are nearly identical.

Samples C, D, E, F, G. The experimental FT magnitudes and fits for samples **C**, **D**, **E**, **F**, and **G** and the corresponding Fourier-filtered data are shown in Figure 5. All spectra exhibit features similar to those of samples **A** and **H** described in the preceding paragraph. This is also reflected by the fit parameters listed in Table 2. However, a certain trend can be discerned going from sample **C** (1 mM Pu(IV) at −log [H^+] 0.56) to the precipitate sample **H**. The apparent splitting of the oxygen neighbor shell due to the inherent disorder in the colloidal hydroxide particles initially increases, to then decrease again with increasing −log [H^+]. This trend is also reflected by the shape of the oxygen peak in the FT spectra (Figure 5, left panel). The Pu second next-neighbor coordination number observed for the solution samples **C** through **G** increases with increasing −log [H^+].

Sample **C** at the onset of polynucleation and the precipitate sample **H** show a single oxygen distance value similar to that expected for PuO_2(cr) (2.33 Å). The mean square radial displacement is increased (and, hence, the apparent coordination number drops) for the amorphous solid. For samples **D**−**F** the nearest neighbor oxygen metrical parameters are grouped in a minor contribution at a shorter (2.20−2.24 Å) and a major contribution at a longer (2.38−2.42 Å) distance. This ratio seems to be reversed for the high concentration stock solution **A**. In the case of sample **G**, the distance differences between the shells O1 and O2 has decreased to 0.08 Å (2.29 and 2.37 Å, with a mean value of 2.33 Å). The Pu second next-neighbor positions obtained for samples **A** and **C**−**H** only slightly vary between a 3.86 and 3.90 Å distance from the absorber and seem to be barely affected by the disorder fluctuations present in the oxygen nearest neighbor shell. We observe Pu−Pu distances that are 0.05 to 0.09 Å elongated compared to the theoretical value of 3.81 Å for PuO_2(cr). Our results are visualized in Figure 6, where the coordination numbers obtained for the individual shells are plotted against the corresponding distance values for samples **A**−**H**.

XANES Results. The normalized XANES spectra for samples **B**, **C**, **E**, **F**, and **H** are depicted in Figure 7. No shift in the energy of the XANES WL is evident in any of the spectra, nor is there any structure at the high energy side of the WL characteristic for actinyl dioxo moieties, testimony for all samples being in the tetravalent state. An example of a fit result to the XANES, performed as described in the

(25) Ankudinov, A. L.; Conradson, S. D.; Mustre de Leon, J.; Rehr, J. J. *Phys. Rev B* **1998**, *57* (13), 7518−7525.

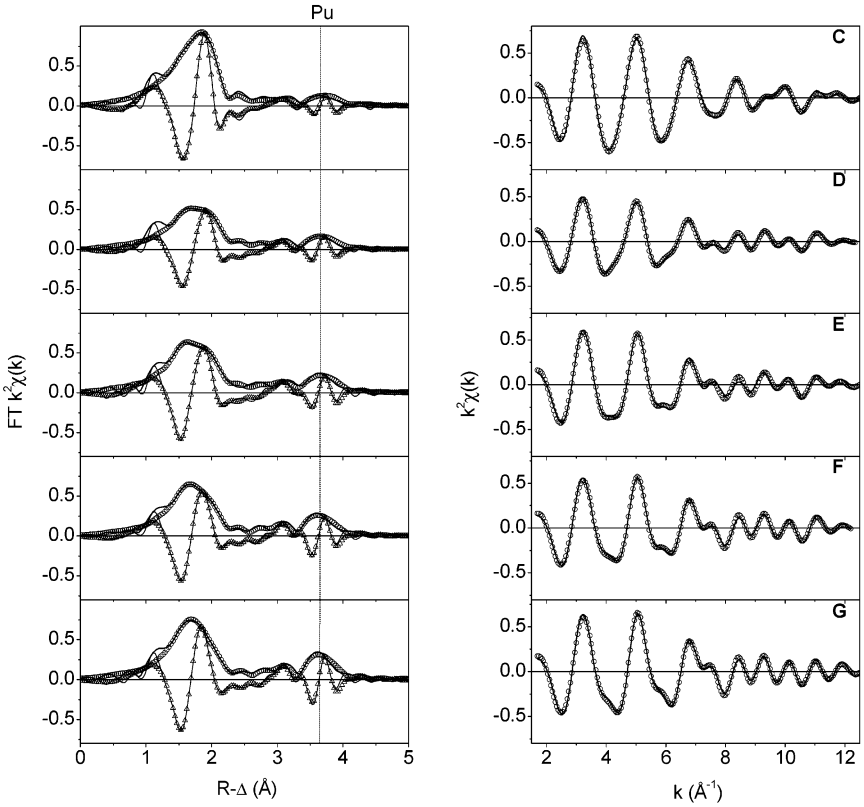

Figure 5. *R*-space fit results for aqueous colloidal suspension samples (**C**, **D**, **E**, **F**, **G**). Left panel: FT magnitude of EXAFS data (solid line), fit magnitude (open circles), FT imaginary part (thin solid line), and fit imaginary part (open triangles). Right panel: corresponding Fourier-filtered data (solid line, ranges given in Table 2) and back-transformed fit (open circles). Dashed line marks Pu−Pu interaction.

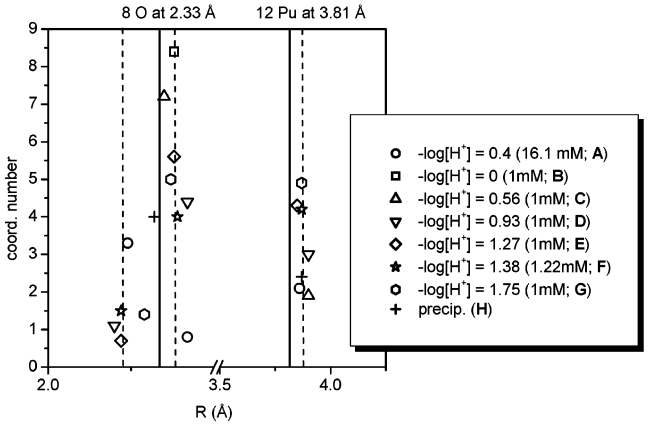

Figure 6. Graphical representation of EXAFS metrical parameters for samples **A** through **H**: coordination numbers N_i plotted vs interatomic distances R_i (see text for details). Solid vertical lines mark theoretical PuO_2 first and second next Pu neighbor distances.

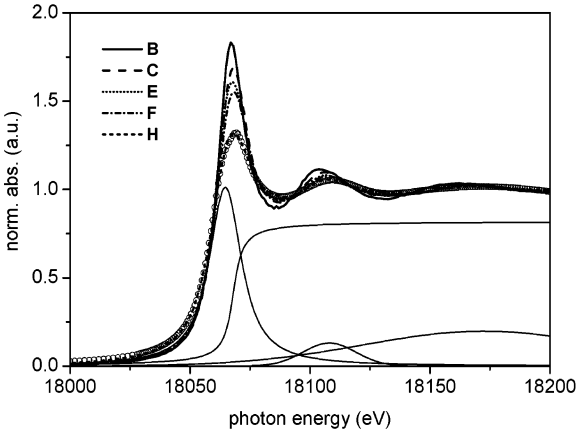

Figure 7. Pu L3 edge XANES spectra for Pu^{4+}(aq) (**B**), Pu(IV) hydroxide colloids (**C**, **E**, **F**), and precipitated $Pu(OH)_4$(am) (**H**), including least-squares fit (open circles) and fit components for sample **H** (see text for details).

Experimental Section, for sample **H** is shown in the same figure. A significant change in the intensity of XANES features is observed, which is predominant for the WL. The WL intensity decreases going from the Pu^{4+} aquo ion (**B**) to the amorphous $Pu(OH)_4$(am) precipitate (**H**). Figure 8 shows that there is an almost linear correlation between the decrease of WL peak height (determined as the pseudo-Voigt profile height in the XANES fit result) and $-\log [H^+]$. Note that the pseudo-Voigt profile area, reflecting the integral $2p_{3/2} \rightarrow 6d$ transition probability, remains constant for all samples. Sample **A** and the solid $Pu(OH)_4$(am) sample **H** exhibit the lowest WL intensities.

Discussion

EXAFS. The metric parameters obtained for 1 mM Pu(IV) at $-\log [H^+]$ 0 (sample **B**) fully agree with results obtained in previous EXAFS investigations of the Pu^{4+} aquo ion.[25] Eight to nine water molecules (depending on the uncertainty in the S_0^2 value) coordinate Pu(IV) at a 2.38 ± 0.02 Å Pu−O bond distance.

The highly asymmetric oxygen coordination in the colloid samples **A** and **C**−**G** and the amorphous precipitate **H** unambiguously indicates the presence of different Pu−O bond lengths from different coordinating oxygen atoms ($-O^-$, −OH, OH_2). However, we cannot use these metric

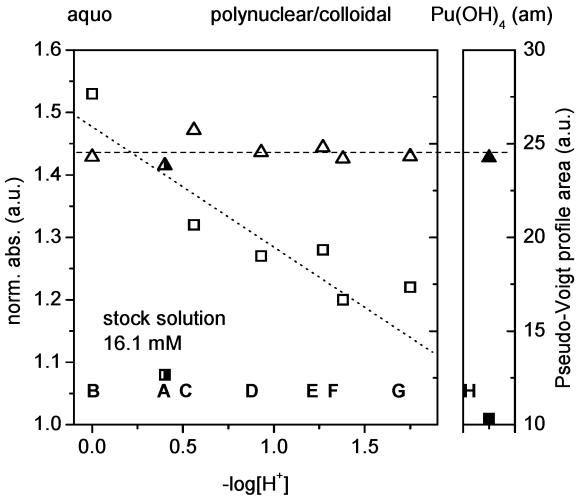

Figure 8. Pseudo-Voigt profile height (squares) as a measure of the white line intensity and integrated area (triangles) from fit results to the XANES for samples **A**−**H**. Sample **A** is marked with a different symbol to accentuate its different behavior, as it is an oversaturated solution.

parameters obtained specifically for formulating a precise structure model, as does Conradson.[1] This is because the bond length resolution in EXAFS is limited by $\Delta R \approx \pi/2k_{max}$ and is 0.13 Å in this study. This renders it difficult, and for some distances impossible, to separate contributions from multiple, closely spaced backscatterers. We can and will further below, however, postulate a model of colloid growth, which agrees with the trends in the EXAFS and XANES data, combined with LIBD and UV/vis spectroscopy results.

In the case of samples **D**−**G** one can observe the splitting between a dominant oxygen contribution at average distances slightly larger than that for PuO_2(cr) and a smaller contribution at a significantly shorter distance (around 2.22 Å). Only for sample **A**, the colloids formed in the more concentrated stock solution, the short distance contribution seems to be dominant. In agreement with refs 1 and 26, we assign this shorter Pu−O distance to hydroxyl groups. The Pu−Pu distances remain hardly influenced by the splitting in the nearest neighbor oxygen shell, supporting the hypothesis of the presence of a rather rigid −Pu−O−Pu− "backbone" in the nanoparticle lattice as the basis of the polynuclear and/or colloidal Pu(IV) hydrolysis species. This is also corroborated by FEFF8.2 simulations presented in Figure 9. In this figure a 45-atom fluorite structure simulation of the PuO_2(cr) EXAFS (top row) is compared to results obtained for a defect and distorted cluster (bottom row), where Pu voids in the Pu sublattice represent Pu defect sites. The agreement between the simulation and the EXAFS of the colloid species (e.g., sample **F**) is highly convincing.

XANES. There are two possible explanations for the WL intensity variations observed in the XANES regime. As already pointed out in our previous investigation of Th(IV) hydrolysis products,[27] one is an extrinsic effect, resulting from charge transfer, and the other an intrinsic effect, resulting from the variation in particle size. The WL feature is associated with a dipole allowed transition from a $2p_{3/2}$ core level into an empty 6d state, lying just above the continuum. Changes in the intensity of the WL can result from variations in the occupancy of d states caused by charge transfer between the central absorbing atom and its surrounding nearest neighbors, an extrinsic effect (e.g., refs 28 and 29). Intrinsic particle size effects leading to variations in L3 XANES WL intensities have been reported for, e.g., spectra of metallic nanoparticles (e.g., ref 30). The WL intensity variation, in this case, results from variation of the density of state (DOS) for atomic clusters as a function of the number of atoms in the cluster or the ratio of surface atoms to atoms in the bulk.

No significant variation in WL area, determined from least-squares fits to the data, is observed for the Pu(IV) samples (see Figure 8). The integral transition probability remains constant, excluding any charge transfer to the d-like final states. Again we conclude that the WL intensity variation is likely a particle size effect similar to that reported in ref 27. Of all the Pu(IV) samples investigated here, the Pu^{4+} aquo ion can be assumed to have the most molecular orbital (MO)-like 6d final state. Because the $2p_{3/2} \rightarrow$ 6d dipole allowed transition probability (or square root of the absorption coefficient) is proportional to the energy-dependent density of the 6d final states, the MO-like, more localized final state has the greatest transition probability of these samples and, hence, largest WL intensity. The 6d state of the condensed amorphous $Pu(OH)_4$(am) precipitate is better described as a band than as a discrete MO. The density of the 6d-like final state is spread over a larger energy interval. With it, the height of the WL is observed to be lower than for all other samples, due to the subsequent lower transition probability. At the same time, the width of the WL feature increases significantly (Figure 7). The colloid samples **C**−**G** represent an intermediate situation. Here the particle size, as reflected by the decreasing WL height, increases with increasing $-\log [H^+]$. If small Pu colloid species exhibit 6d-like final states intermediary between the MO picture used for the aquo ion and the band structure picture describing the condensed system of sample **H**, the DOS of the colloids should tend toward that of a bulk sample's band structure for large clusters. This is obviously the case. Note that the WL height for sample **A**, which is at a strong oversaturation Pu(IV) concentration above the solubility limit, approaches that for the $Pu(OH)_4$(am) precipitate **H**. The interpretation of WL height decrease to result from photoelectron scattering on an increasingly disordered crystal lattice, as proposed by Conradson et al.,[31] does not hold here. The WL decrease in Figure 7 must be related to increasing particle size, as the EXAFS results demonstrate this decrease in WL height to be also associated with an increase in the ordering of the

(26) Denecke, M. A.; Marquardt, C. M.; Rothe, J.; Dardenne, K.; Jensen, M. P. J. *Nucl. Sci. Technol.* **2002**, *3*(Suppl.), 410−413.
(27) Rothe, J.; Denecke, M. A.; Neck, V.; Müller, R.; Kim, J. I. *Inorg. Chem.* **2002**, *41*, 249−258.
(28) Mansour, A. N.; Cook, J. W., Jr.; Sayers, D. E. *J. Phys. Chem.* **1984**, *88*, 2330−2334.
(29) Lee, Y. S.; Whang, C. N.; Jeon, Y.; Choi, B. S.; Han, T. J.; Woo, J. J.; Croft, M. *Nucl. Instrum. Methods Phys. Res. B* **1997**, *129*, 387−391.
(30) Bazin, D.; Sayers, D.; Rehr, J. J.; Mottet, C. *J. Phys. Chem. B* **1997**, *101*, 5332−5336.

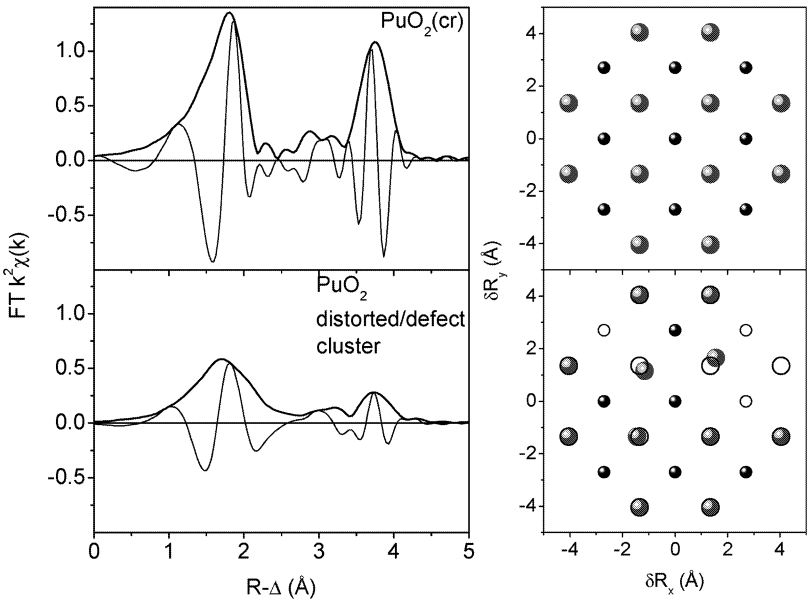

Figure 9. FEFF8.2 calculations for 3-shell fluorite structure PuO_2 cluster (left panel, top) and distorted cluster with defect sites (left panel, bottom) simulating local structure in the colloid samples. The right panel shows the projection of the clusters along the Cartesian *z*-axis. Small dark spheres represent metal cations, large spheres oxygen atoms, and circles "voids" or defect sites. See text for details.

−Pu−O−Pu− backbone structure of the colloids. It is also associated with an increase in order of the oxygen neighbor shell for solution samples at the highest −log [H^+]. The decrease in WL height is, hence, not associated with increasing disorder.

LIBD. Observation of colloid formation in the LIBD experiments is evidence for exceeding the solubility limit. Macroscopically, the solubility limit is defined as the concentration where the total amount of a substance is no longer present in ionic form but instead forms a precipitate. The "precipitate" found in the LIBD experiment is colloids, which are so small that they remain suspended due to Brownian motion. Plotted in Figure 1 (solid line) is the solubility curve of Pu(IV) according to ref 32 along with experimental errors (dashed lines) for

$$\log K^{\circ}_{sp} = (\log [Pu^{4+}])(\gamma_{Pu}) + 4(\log [OH^-])(\gamma_{OH}) = -58.7 + -0.3$$

the γ values being the ion activity coefficients. The points of colloid formation observed from LIBD (sample **2** and filled triangles) all lie close to the lower limit of the log K°_{sp} curve indicated. This might be expected since this nanoscopic LIBD approach for solubility determinations is more sensitive than most classical methods. A detailed description how to obtain solubility data from the LIBD experiments by using ion activity coefficients and hydrolysis constants is presented, e.g., in ref 33.

Clues to the formation mechanism of the colloids may also be extracted from this data. It is well-known that Pu(IV) undergoes hydrolysis even under very acidic conditions. For a HCl/NaCl solution of 0.5 M ionic strength and −log [H^+] 0.6, $Pu(OH)_1^{3+}$ and $Pu(OH)_2^{2+}$ should account for more than 80% of the solvated Pu(IV). The remaining 20% is Pu^{4+} aquo ion species, as calculated from the hydrolysis constants of Metivier et al.:[34]

$$Pu^{4+} + 2H_2O \leftrightarrow Pu(OH)_2^{2+} + 2H^+ \quad (1)$$

Colloids may form according to a generalized reaction

$$Pu(OH)_2^{2+} + 2H_2O \leftrightarrow Pu(OH)_{4(coll)} + 2H^+ \quad (2)$$

with $Pu(OH)_{4(coll)}$ designating the presumably oxyhydroxide complex $Pu_nO_p(OH)_{4n-2p}(H_2O)_z$ ($0 \le p \le 2n$). The presence of different oxygen atom types coordinating Pu(IV) indicated in the EXAFS results agrees with the formulation $Pu_nO_p(OH)_{4n-2p}(H_2O)_z$. The expression for the reaction for colloid formation according to reaction 2 is in agreement with the fact that the points of colloid formation in Figure 1 show a linear dependence on −log [H^+] with slope −2. The slope analysis alone only gives information on the ratio between the stoichometric coefficients of Pu(IV) and OH^- and does not allow one to distinguish between the mononuclear $Pu(OH)_2^{2+}$ and any polynuclear species of the form $[Pu(OH)_2]_n^{2n+}$ as actual reactant for colloid formation. However, additional information may be drawn from UV/vis investigations. We have spectroscopically detected a decrease in solvated Pu(IV) species considerably below the solubility limit, which is given in Figure 1, without any observable increase in another Pu oxidation state. The decrease in absorption cannot be due to hydrolysis, since

(31) Conradson, S. D.; Abney, K. D.; Begg, B. D.; Brady, E. D.; Clark, D. L.; den Auwer, C.; Ding, M.; Dorhout, P. K.; Espinosa-Faller, F. J.; Gordon, P. L.; Haire, R. G.; Hess, N. J.; Hess, R. F.; Keogh, D. W.; Lander, G. H.; Lupinetti, A. J.; Morales, L. A.; Neu, M. P.; Palmer, P. D.; Paviet-Hartmann, P.; Reilly, S. D.; Runde, W. H.; Tait, C. D.; Veirs, D. K.; Wastin, F. *Inorg. Chem.* **2004**, *43*, 116−131.
(32) Knopp, R.; Neck, V.; Kim, J. I. *Radiochim. Acta* **1999**, *86*, 101−108.
(33) Neck, V.; Müller, R.; Bouby, M.; Altmaier, M.; Rothe, J.; Denecke, M. A.; Kim, J. I. *Radiochim. Acta* **2002**, *90*, 485−494.
(34) Metivier, H.; Guillaumont, R. *Radiochem. Radioanal. Lett* **1972**, *10*, 27.

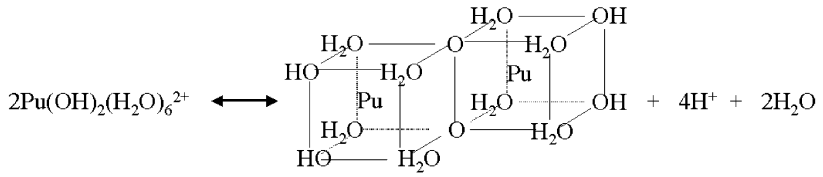

Figure 10. Hydrolysis and condensation of two monomeric $Pu(OH)_2(H_2O)_6^{2+}$ units to an edge sharing, charge-neutral, binuclear species.

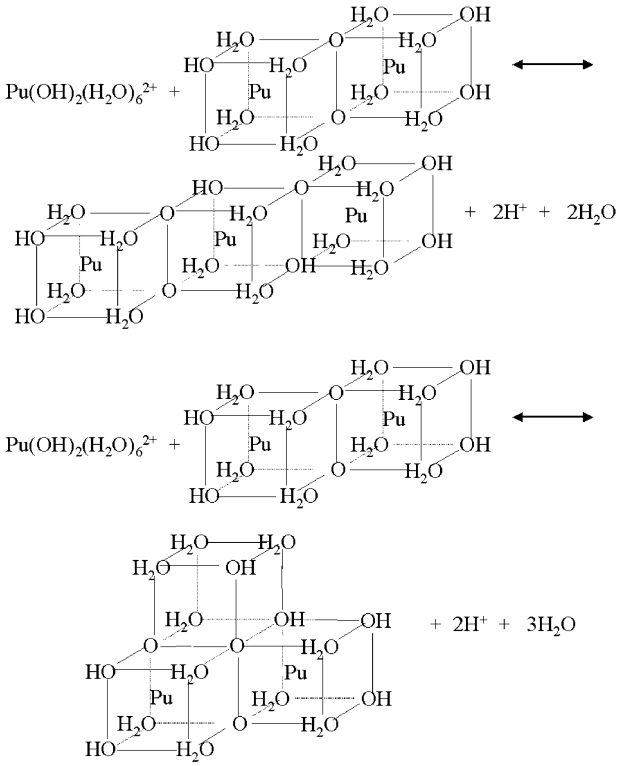

Figure 11. Formation of a trinuclear species through hydrolysis and condensation of a monomeric $Pu(OH)_2(H_2O)_6^{2+}$ unit with a binuclear species to form a single edge sharing, charge-neutral species as product (top) or a double edge sharing species with a common corner (bottom).

the optical absorption coefficient of Pu(IV) remains constant for all $Pu(OH)_n^{4-n+}$ complexes. Polynuclear species, however, do not exhibit strong spectral absorption features, and the decrease in signal is attributed to formation of small polynuclear oligomers, formed by a fraction of the Pu(IV). We will return to this fact in the discussion of our model for colloid growth. Two examples of the simplest of such oligomers (binuclear and trinuclear neutral species) are depicted in Figure 10 and Figure 11. With increasing $-\log [H^+]$, above the initial absorption decrease, a further decrease in the UV/vis absorption is observed, eventually leading to a complete disappearance of the Pu(IV) peak, which is due to quantitative formation of colloids, verified by LIBD. This behavior is analogous to measurements on Np(IV) with laser-induced photoacoustic spectroscopy (LIPAS).[35] Combined LIBD and UV/vis results give the following picture: colloid formation is preceded by formation of small polynuclear species, too small to be detected by LIBD (<5 nm), but causing the first UV/vis absorption decrease. A subsequent growth process with increasing $-\log [H^+]$ leads to the formation of colloids larger than 5 nm, which are detectable directly by LIBD.

Analogous LIBD solubility experiments on tetravalent thorium[36] proved the emerging colloids to be long term stable species, the size of which is determined by the amount of oversaturation of the solution (corresponding to the relative vertical distance from the solubility curve in Figure 1). A similar behavior for fresh Pu(IV) colloids follows from Figure 2. The mean colloid size increases from 12 nm in sample **2** to almost 25 nm in sample **5**. We cannot determine the structure of these colloids directly from the LIBD data, however. Lloyd et al.[37] suggested a cubic fluorite structure, inferring the chemical state $n(PuO_2)$, which is in contradiction with the equilibrium of these colloids with a $Pu(OH)_n^{(4-n)+}$ species. Fujiwara et al.[2] suggest formation of polynuclear species $Pu_{4n}O_{2n}(OH)_{12n}(H_2O)_{4n+5}$, which grow in a stepwise fashion from $Pu(OH)_4(H_2O)_4$ units under loss of water. Their model of colloid growth ultimately leads to PuO_2(cr) formation. Because we cannot explain the LIBD experimental results by the formation of colloids consisting of pure crystalline particles, as it would contradict the observed -2 slope, the polynuclear oligomers formed at low $-\log [H^+]$ below the solubility limit may serve as cores or crystallization centers for colloid formation, which become covered by an amorphous hydroxide layer when the solubility for $Pu(OH)_4$ is exceeded. The growth of an amorphous hydroxide layer would fulfill the slope -2. It would, however, contradict our EXAFS findings that show the structural order of the colloids to increase with size. That small PuO_2 oligomers form is supported by the findings of Kim et al.,[4] who measured a solubility product of PuO_2 (log [Pu] -3.6, 1 M $HClO_4$), 2 orders of magnitude lower than for $Pu(OH)_4$ (log [Pu] -1.5, 1 M $HClO_4$), and could not separate the colloidal fraction by filtration, probably due to their small size.

We now compare these proposed mechanisms of colloid formation with the EXAFS results. Sample **B**, well below the solubility of $Pu(OH)_4$ and at $-\log [H^+]$, where the mononuclear (hydrated) Pu^{4+} dominates (less than 50% hydrolyzed species), shows a single oxygen shell due to eight coordinated water molecules. No Pu−Pu interaction is observed, since there are little or no polynuclear species, further confirmed by UV/vis spectroscopy. The EXAFS sample **A** contains solvated $Pu(OH)_n^{(4-n)+}$ species along with a large fraction of colloids. Due to the strong oversaturation of solution **A** with respect to the solubility curve given by the LIBD experiments, the appearance of its UV/vis spectrum (not shown), and the XANES results, the colloids most likely are large in size and are composed of amorphous

(35) Neck, V.; Kim, J. I.; Seidel, B. S.; Marquardt, C. M.; Dardenne, K.; Jensen, M. P.; Hauser, W. *Radiochim. Acta* **2001**, *89*, 439−446.
(36) Bitea, C.; Müller, R.; Neck, V.; Walther, C.; Kim, J. I. *Colloids Surf. A* **2003**, *217*, 63−70.
(37) Lloyd, M. H.; Haire, R. G. *Radiochim. Acta* **1978**, *25*, 139.

$Pu(OH)_4$(am) or at least have a thick outer layer of $Pu(OH)_4$(am). The dominance of the short Pu−O distance associated with ligated hydroxyl groups and a small coordination number for the Pu shell in this sample's EXAFS, similar to that observed for the amorphous $Pu(OH)_4$(am) precipitate (sample **H**), can be considered to support the conclusion that the colloids in **A** are $Pu(OH)_4$(am)-like.

Samples **C** through **G** show a trend toward increasing Pu coordination number up to N_{Pu} 4.9, while the Pu−Pu distance remains between 3.85 and 3.90 Å. The apparent order in the sample Pu sublattice increases with increasing $-\log [H^+]$ and colloid size. A mechanism of colloid formation and growth from agglomeration of ordered oligomers is consistent with the observed increase in Pu sublattice order; simple growth of a wholly amorphous layer on core centers is not. As we have shown, the presence of oligomers is indicated by the UV/vis absorption decrease. If a mechanism involving growth of an amorphous layer on core centers were valid, then the trend of the colloids from samples **C** to **G** should approach that of sample **H**, the amorphous precipitate. The Pu sublattice of sample **H** is presumably more disordered, as reflected in the fit value for N_{Pu} 2.4. The colloid solution samples do not become more disordered but more ordered as their size increases. An agglomeration of crystalline PuO_2 oligomers for colloid growth ($n(PuO_2)$) could explain the observed increase in Pu sublattice order with increasing particle size in the solution samples. However, this model is inconsistent with both the observed −2 slope of the LIBD solubility curve in Figure 1, with the observed splitting of the Pu−O coordination sphere (Table 2), and with the simulation presented in Figure 9, indicating the presence of defect sites in the Pu sublattice. The EXAFS analysis also indicates that −OH ligands are present in the colloid containing samples at relatively short distances. If the colloids were a cubic fluorite structure of $n(PuO_2)$, we would not expect the −OH distance to be observed throughout.

We propose a model of eigen-colloid formation, which is consistent with the XAFS, LIBD, and UV/vis data and similar to the model of Fujiwara et al.[2]. We envisage Pu(IV) eigen-colloid formation through growth and agglomeration of small oxyhydroxide $Pu_nO_p(OH)_{4n-2p}(H_2O)_z$ oligomers, which themselves form through condensation of monomeric units. For the model to be consistent with XAFS, LIBD, and UV/vis data, monomeric solvated Pu(IV) species must disappear before colloids >5 nm actually form, and colloid formation must entail splitting of the nearest-neighbor oxygen shell, provide for the presence of a −Pu−O−Pu− backbone having a face-centered cubic (fcc) Pu sublattice in the colloid structure, whose static order increases with colloid size, and involve a −2 slope dependency on solubility versus $-\log [H^+]$. The following model of Pu(IV) oxyhydroxide colloid formation through growth and agglomeration of small oligomers fulfills these requirements.

Let us begin by picturing condensation of monomeric units to form oligomers in our scheme of eigen-colloid formation. We consider here the smallest and simplest possible oligomers, binuclear and trinuclear species formation from monomeric units. These are the simplest and, hence, easiest to visualize. They also represent the smallest building blocks, from which we may conceive building the colloid structure. Consider a reaction of hydrolysis coupled with condensation of two monomeric species to form a dimer of cubic units connected at their edges:

$$2Pu(OH)_2(H_2O)_6^{2+} + xH_2O \leftrightarrow Pu_2O_p(OH)_{8-2p}(H_2O)_{6+p} + 4H^+ + (2+x)H_2O \quad (3)$$

An example of reaction 3 to one of the possible products ($p = 2$) is depicted in Figure 10. The units are connected at their edges, because a Pu−Pu distance near that observed in the EXAFS results; joining them at their faces or at their corners would result in distances too short or too long, respectively. We choose to formulate reaction 3 using the octacoordinate monomer as reactant, as EXAFS results suggests an average Pu(IV) coordination number of eight at low $-\log [H^+]$. Using a number of water molecules coordinating the monomeric charged species other than eight would merely change the stoichiometry factor for the number of water molecules in reaction 3. We also choose hydrated $Pu(OH)_2^{2+}$ as the reactant as it fulfills the −2 slope dependency needed to be in agreement with LIBD results. In reaction 3, oxide bridge links may form via the condensation reaction equivalent $2OH^- \leftrightarrow H_2O + O^{2-}$. The number of oxide links from this special condensation reaction is "*p*" in reaction 3.

Note that reaction 3 is a generalized reaction scheme for binuclear species formation. The actual mechanism may proceed by initial hydrolysis of monomeric units according to

$$Pu(OH)_2(H_2O)_6^{2+} \leftrightarrow PuO_p(OH)_{4-2p}(H_2O)_{4+p} + 2H^+$$

with subsequent condensation to $Pu_2O_p(OH)_{8-2p}(H_2O)_{6+p}$ under loss of two water molecules. It may also proceed via condensation of $Pu(OH)_2(H_2O)_6^{2+}$ units followed by release of protons to lower charged or noncharged species:

$$2Pu(OH)_2(H_2O)_6^{2+} \leftrightarrow Pu_2(OH)_4(H_2O)_{10}^{4+} + 2H_2O \leftrightarrow (p+x)H^+ + Pu_2O_p(OH)_{4-p+x}(H_2O)_{10-x}^{(4-p-x)+}$$

with $x \le 4$ and $p \le 4 - x$. This process would also fulfill the Pu(IV):OH^- ratio of 2 expected from LIBD results.

In visualizing formation of the next higher polynuclear species, a trinuclear species from a binuclear species and an additional monomeric unit (in effect equivalent to reaction of three monomeric units), we must again keep in mind that ultimately a fcc Pu sublattice with an approximate 3.87 Å distance between Pu atoms should form. This is possible through connection of a third monomeric $Pu(OH)_2(H_2O)_6^{2+}$ unit to a dimer either in the same pattern as for the formation of the binuclear complex (i.e., attachment along cube edges to form a chain with general formula $Pu_nO_p(OH)_{4n-2p}(H_2O)_{2n+2+p}$) leading to a $Pu_3O_p(OH)_{12-2p}(H_2O)_{8+p}$ species, or by attaching a third monomeric $Pu(OH)_2(H_2O)_6^{2+}$ unit along two edges of neighboring cubes of a dimer, resulting in a trimer of cubes

sharing one common corner, $Pu_3O_p(OH)_{12-2p}(H_2O)_{7+p}$. Examples of these two possibilities for the formation of trimers (both with $p = 3$) are shown in Figure 11. As for the dimer reaction, it is feasible that the actual mechanism involves hydrolysis with subsequent condensation, condensation of charged species followed by release of protons, or any combination thereof. It is not possible to say from our data which mechanism actually occurs, in what order, or if it occurs stepwise at all. The central factor in this scheme is that the structure of growing oligomers occurs in a manner resulting in Pu−Pu distances near 3.87 Å, that small oligomers form, as indicated by UV/vis results, and that the Pu(IV):OH^- ratio of 2 is adhered to.

We can imagine that growth to larger oligomers proceeds by condensation of dimeric and trimeric units either with one another or with other monomeric units, thereby uniting their cube edges. If we imagine continued linking together of such units at their edges in all dimensions, ultimately a fcc arrangement of Pu(IV) cations forms. This represents the Pu sublattice or −Pu−O−Pu− backbone in the colloid particle structure, in accord with our EXAFS results. The elongation of the Pu−Pu distance in the colloids over that for PuO_2(cr) observed in the EXAFS can be considered to result from the larger size of the hydrated primary building blocks comprising the colloids, compared to $Pu(O)_8$ cubic building blocks of the crystalline compound.

Note that the formation of polymeric oligomers via condensation of monomeric units at their corners or cube faces is also feasible. However, the Pu sublattice of the resulting oligomers is no longer fcc. Such reactions may be the source of the defects in the Pu sublattice (cf. Figure 9 and related discussion). Introduction of a corner sharing polymer into a growing edge sharing oligomer breaks up the fcc Pu sublattice, because the unlike polymers do not fit together in a manner similar to matching puzzle pieces. This would lead to empty cubes or Pu defect sites. If the reader has ever played the computer game 3D Tetris, he or she can easily visualize how "lock and key" fitting of cubes connected in different fashions (at corners versus at their edges) into a three-dimensional network can affect holes in the structure. These holes or empty cubes could represent the defects in the colloid Pu sublattice observed in the EXAFS and whose presence is corroborated through the simulation presented in Figure 9. Attachment of units along their faces appears less likely, as this would result in interstitial Pu atoms in the fluorite fcc structure, as opposed to defect "holes" in the structure, as well as to a Pu−Pu distance much shorter than that observed.

Conclusions

The present paper describes the first combined XAFS/LIBD investigation of the formation and structure of Pu(IV) oxyhydroxide eigen-colloids in aqueous suspension. On the basis of our XAFS and LIBD results, a model for colloid formation via condensation of $Pu_nO_p(OH)_{4n-2p}(H_2O)_z$ oligomers is put forward. The resulting structure exhibits a −Pu−O−Pu− backbone with increasing order as the size of the colloids increase. The Pu−O coordination shell shows a variable degree of order, likely due to the variation in numbers of O^{2-}, OH^-, and H_2O ligands in the growing structural network. The highest degree of order is in the largest colloids (sample **G**), where the highest degree of condensation, correlated to the greatest degree of O^{2-} bridging in the cubic network, might be expected.

Further investigation is needed in order to corroborate this hypothetical model of colloid growth. Our data does not directly reveal the structure of the small oligomers formed. We postulate the structural compostion being cubic units, as this represents the basic units or building blocks comprising the larger colloids, which our EXAFS results indicate to have an ordered Pu−O−Pu− backbone fcc structure. The oligmers in reality may have a much different structure, which somehow totally reorganizes upon growth and agglomeration to colloids. Simultaneous LIBD and XAFS experiments and quantum chemical calculations of the stability of different oligomers will be performed. In addition, an alternative mechanism of increasing numbers of small polymeric, well-ordered solution species and simultaneous increasing size of amorphous colloids could also be considered to be in accord with our combined EXAFS and LIBD results. In order to differentiate between these two mechanisms, we will perform XAFS experiments on colloids filtered off the solution samples and on their filtrates in the future. Finally, experiments are now underway aimed at providing a reason for the decrease in amplitude for the Pu−Pu interaction in the $Pu(OH)_4$(am) precipitate (sample **H**) that otherwise is observed to increase with increasing colloid size in the solution samples **C**−**G**.

Acknowledgment. We thank Dr. A. Seibert for the preparation of sample **B**, Drs. K. Dardenne, P. Lindqvist-Reis, P. Panak, and A. Seibert for aiding in XANES/EXAFS data acquisition, and C. Bitea and Drs. C. Marquardt and V. Neck for assistance in planning and performing LIBD studies. Use of the APS was supported by the U.S. Department of Energy, Office of Science, Office of Basic Energy Sciences, under Contract No. W-31-109-ENG-38. We are grateful for beamtime allotment and experimental assistance by BESSRC and the BESSRC beamline staff and by the ESRF and the ROBL staff. Use of the infrastructures of the Actinide Facility for synchrotron research in the Chemistry Division of ANL and support by Chemistry Division staff is also acknowledged with gratitude.

IC049861P